Respiratory-resolved MR-based attenuation correction for motion-compensated cardiac PET-MR

Christoph Kolbitsch[1,2], Radhouene Neji[2,3], Matthias Fenchel[4], Andrew Mallia[2], Paul Marsden[2], and Tobias Schaeffter[1,2]

[1]Physikalisch-Technische Bundesanstalt (PTB), Braunschweig and Berlin, Germany

[2]King's College London, Division of Imaging Sciences and Biomedical Engineering, London, UK

[3]MR Research Collaborations, Siemens Healthcare, Frimley, UK

[4]MR R&D Collaborations, Siemens Medical Solutions, New York, USA

Corresponding author:

Christoph Kolbitsch, Physikalisch-Technische Bundesanstalt (PTB), Abbestraße 2-12, 10587 Berlin, Germany, E-mail: christoph.kolbitsch@ptb.de

Short running title:

Dynamic MR-AC for cardiac MR-PET

Word count: 5000

Respiratory motion during cardiac PET acquisitions can cause image blurring and erroneous uptake quantification. Especially the misalignment of attenuation correction (AC) maps and PET emission data can lead to severe quantification errors, because the AC value of the heart is five times higher than of the surrounding lung tissue. Standard PET-MR approaches assume accurate alignment between breathhold MR-based AC maps and free-breathing PET emission data but cannot necessarily ensure it.

Here we propose a 75-seconds free-breathing MR-acquisition, which provides respiratory-resolved AC maps (AC_{Dyn}) and non-rigid respiratory motion information. This approach ensures accurate AC for free-breathing PET data and the motion information can be utilized to reduce image blurring caused by respiratory motion.

Methods: 3D multi-echo MR data was acquired during a 75-seconds free-breathing scan in six patients. Both a respiratory-resolved dynamic AC map (AC_{Dyn}) and a non-rigid respiratory motion field are provided by the MR scan. AC_{Dyn} yielded AC values for different breathing phases ensuring accurate AC for each respiratory phase of the free-breathing PET data. In addition, motion-corrected image reconstruction (MCIR) of MR and PET data was used to minimize breathing artefacts.

Results: motion amplitudes in the left ventricle were 8.2 ± 2.9mm with a dominant motion direction along the anterior-anterolateral and inferior-inferoseptal axis of the heart. The proposed AC_{Dyn}-MCIR technique led to significant signal recovery of PET tracer uptake by 24 ± 5% ($p<0.05$). The maximum improvement was observed in patients with large misalignment between standard breathhold MR-based AC maps and PET emission data. PET image resolution was improved by 20 ± 12% ($p<0.05$).

Conclusion: We have presented an efficient MR-scan, which ensures accurate motion information and AC values to improve PET quantification for cardiac PET-MR scans. The short scan time of 75 seconds makes this free-breathing acquisition easy to integrate into standard clinical PET-MR protocols.

Keywords: simultaneous PET-MR, motion compensation, respiratory-resolved AC

INTRODUCTION

Cardiac PET is commonly seen as the gold standard for assessing the viability and perfusion of the myocardium (Bengel et al. 2009; Loghin et al. 2004; Schwaiger et al. 2005; Lautamäki et al. 2008). The most common radiotracers used are ^{18}F-FDG, $^{13}NH_3$ and ^{83}Rb but a wide range of other tracers exist which provide additional diagnostic information, making cardiac PET a highly versatile medical imaging modality.

One of the main challenges of cardiac PET is physiological motion of the heart due to breathing, which can lead to two types of errors: (A) The movement of the heart causes blurring of emission data (blurring error). (B) Respiratory motion can lead to a misalignment between the position of the heart in the PET emission scans and in the attenuation correction (AC) maps, which are usually obtained independently. Misalignment between the AC and PET emission data can result in tissue density compensation with the wrong AC values (AC error). This is especially a problem for cardiac PET, because the heart is largely surrounded by lung tissue, which has a five times smaller AC value than myocardium. Falsely correcting uptake in the myocardium with AC values of lung tissue leads therefore to severe quantification errors (Schwaiger et al. 2005; Lautamäki et al. 2008; Nye et al. 2007).

Munoz et al., have recently presented an approach for MR-based respiratory motion correction and showed an improvement in measured uptake in the myocardium in the order of 10% compared to uncorrected images (Munoz et al. 2018). Other PET-MR studies have presented line plots through the myocardium showing similar improvement using respiratory motion correction compared to this study but their quantitative evaluation was focused on tumor uptake (Grimm et al. 2015; Manber et al. 2015). Two PET-CT studies have reported reductions of measured tracer uptake due to respiratory motion blurring of 30% (Boucher et al. 2004; Yu et al. 2016).

For simultaneous PET-MR scans of the thorax or abdomen, AC maps are commonly obtained during a short breathhold scan prior to the free-breathing PET acquisition (Martinez-Moller et al. 2012). A 5min

3D free-breathing AC-MR acquisition scheme has recently been proposed for abdominal motion-corrected PET-MR applications (Kolbitsch et al. 2018). This technique provided dynamic respiratory-resolved MR-based AC maps (AC_{Dyn}) and non-rigid respiratory motion fields (MF), which were utilized in a motion-corrected image reconstruction (MCIR) to compensate for respiratory image artefacts in abdominal MR and PET images. In contrast to gated image reconstructions, PET-MCIR utilizes all acquired counts for image reconstruction while using MF to minimize motion blurring (Qiao et al. 2006). This ensures high image quality with high scan efficiency. The dynamic MR-based AC maps, obtained during free-breathing, showed a much better alignment with the free-breathing PET-MCIR images than the standard breathhold AC maps.

Here we adapted this technique for cardiac PET-MR and assessed the improvement of visualization and quantification in PET images achieved by using respiratory-resolved AC maps and motion-corrected image reconstruction for cardiac PET-MR applications.

METHODS

We used a 75s free-breathing MR scan, which provides respiratory-resolved dynamic AC maps (AC_{Dyn}) for accurate PET quantification. In addition, it yielded respiratory motion information, which can be used in a motion-corrected image reconstruction (MCIR) of the MR and simultaneously acquired PET data to reduce motion artefacts. Figure 1 compares the standard breathhold MR-AC acquisition and the proposed dynamic MR-AC technique. Misalignment errors between AC and PET emission data were avoided and blurring of PET uptake in the myocardium caused by respiratory motion could be minimized. No breathhold for AC acquisition was required and 3D respiratory motion information was directly obtained from the MR-AC scan without the need of an additional scan.

Data acquisition

Simultaneous PET-MR scans were carried out on a 3T PET-MR scanner (Biograph mMR, Siemens Healthcare, Erlangen, Germany). Data acquisition was carried out similarly to a method previously published for respiratory motion correction of abdominal PET-MR scans (Kolbitsch et al. 2018). In order to adapt this approach from abdominal to cardiac applications, image resolution, echo times and total scan times were adapted. Cardiac PET-MR data were acquired for 3:18 min with PET-data in list-mode. Prior to the PET scan a dual-echo Dixon gradient echo (GRE) scan was obtained during a 19 s breathhold to calculate the standard static MR-AC map (AC_{Stat}) with the following scan parameters: coronal orientation, echo times of TE_1=1.23 ms and TE_2=2.46 ms, a repetition time of TR=3.6 ms, flip angle of 10° covering a field-of-view (FOV) of 500 x 328 x 400 mm^3 with a spatial resolution of 2.6 x 4.1 x 3.1 mm^3.

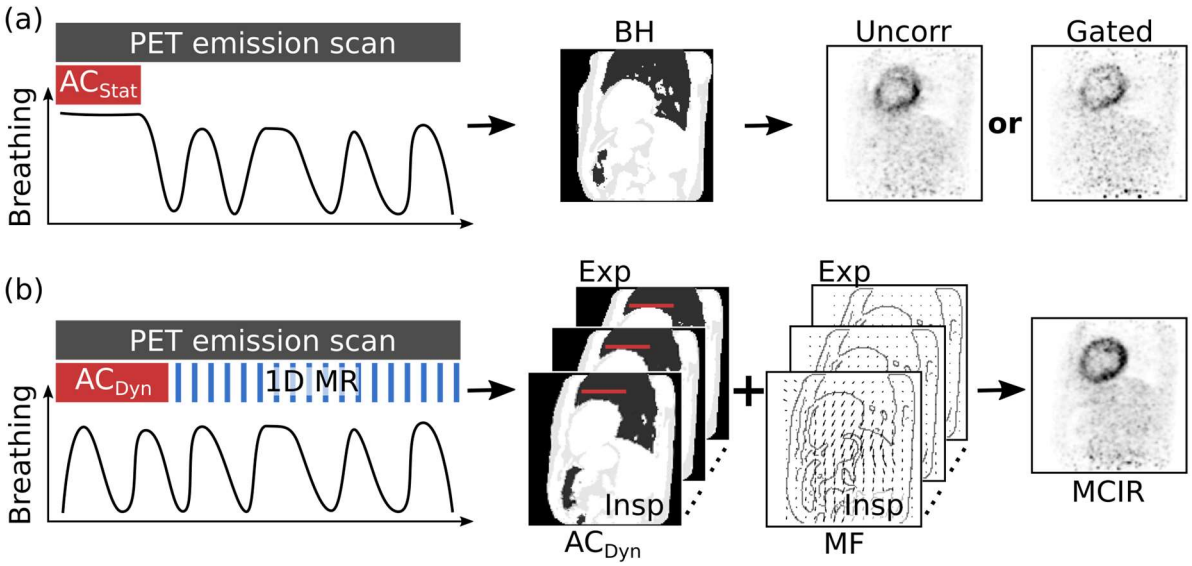

Figure 1: Overview. (a) For the standard approach, a MR-based attenuation correction map (AC_{Stat}) is acquired during a breathhold (BH) at the beginning of the simultaneous PET scan yielding a single 3D AC volume. An uncorrected (Uncorr) or a respiratory gated (Gated) PET image can be reconstructed. (b) For the proposed approach the AC information is obtained during free-breathing which yields 3D AC volumes (AC_{Dyn}) for different breathing states from inspiration (Insp) to expiration (Exp) and 3D non-rigid respiratory motion fields (MF). A respiratory surrogate signal is obtained from a 6 ms 1D MR scan acquired every 750 ms (1D MR). This information can then be utilized in a motion-corrected image reconstruction (MCIR) to obtain a high-quality PET image.

For the proposed AC_{Dyn}-MCIR approach a triple-echo Dixon GRE scan with echo times of TE_1=1.23 ms, TE_2=2.72 ms and TE_3=4.21 ms and a repetition time of TR=6 ms with a flip angle of 10° was carried out

in sagittal orientation during free-breathing. The scan time was 75 s. The FOV for this scan was 400 x 400 x 400 mm^3 with a spatial resolution of 1.9 x 3.2 x 3.2 mm^3.

Data acquisition was carried out using a prototype 3D Golden radial phase encoding (GRPE) (Prieto et al. 2010), with readout along the foot-head direction.

GRPE yields high-quality static 3D MR images but also allows for the reconstruction of respiratory self-navigator signals and respiratory-resolved 4D MR images to accurately estimate respiratory motion (Buerger et al. 2013). It has previously been shown to provide accurate anatomic and motion information for a range of different applications (Aitken et al. 2015; Kolbitsch et al. 2017). For more information on this acquisition scheme please refer to the previous paper by Kolbitsch et al. and supplemental figure 1 (Kolbitsch et al. 2018).

Patient population

Six patients (2 females, 52 ± 10 y, 72 ± 13 kg) who did not have any known heart disease were included in this study after they underwent a clinical PET-CT scan for staging or restaging of oncological diseases, including lymphoma, esophageal cancer and lung carcinoma. Patients were injected with 330 ± 29 MBq of ^{18}F-FDG prior to the PET-CT exam and no further tracer injection was carried out. PET-MR data were acquired 162 ± 19 min after radiopharmaceutical injection. The study was approved by our National Research Ethics Service Committee (reference number: 15/LO/0978).

Image reconstruction

Respiratory motion surrogate

GRPE provided a 1D respiratory self-navigator signal from the central point of each radial phase encoding line with a temporal resolution of 750 ms. Principle-Component Analysis (PCA) was applied to extract a respiratory surrogate signal (Pang et al. 2014). The amplitude of that signal was then used

to separate the acquired MR k-space data into eight different respiratory motion states (i.e. respiratory bins). Figure 2 gives an overview of the calculation of the respiratory motion surrogate.

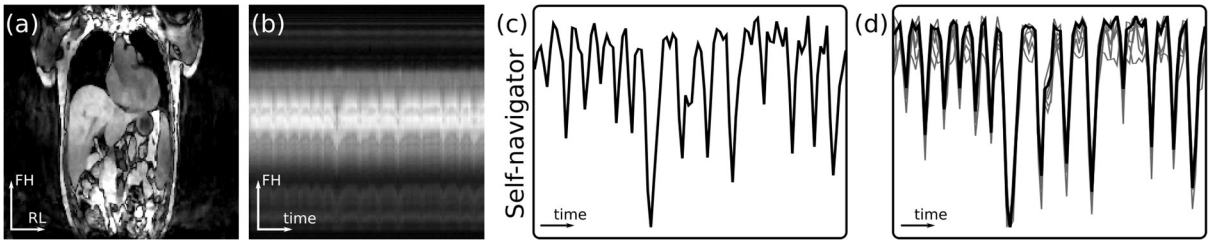

Figure 2: MR-based motion surrogate. (a) Coronal MR image. (b) 1D projection extracted from central k-space lines (i.e. $k_y = k_z = 0$) acquired repeatedly during data acquisition for a single coil. The foot-head (FH) motion of the heart and liver due to breathing can be clearly seen. (c) Respiratory self-navigator signal extracted as first principal component for one coil. (d) Self-navigator signals for all coils (grey lines) and first principle component from all coils (black line) which were then used as the final respiratory surrogate signal.

The MR scan time was shorter than the PET scan time. In order to ensure a reliable motion surrogate for the entire PET acquisition, a central k-space line (i.e. $k_y = k_z = 0$) was obtained every 750 ms after the triple-echo Dixon GRE scan during the remaining PET acquisition.

MR motion estimation

After binning of the MR-data into eight respiratory motion states, an iterative image reconstruction scheme was used to obtain high quality images from the undersampled MR k-space data for each respiratory motion state (Cruz et al. 2016; Kolbitsch et al. 2018). Temporal and spatial total variation regularization was applied to utilize data redundancy between neighboring respiratory bins and minimize aliasing artefacts, yielding eight 3D images describing different respiratory motion states.

Spline-based image registration was performed on these 3D images. Non-rigid motion fields (MF) were obtained by maximizing the mutual information of the image content and adding penalty terms for bending energy (BE) and Jacobian (JAC) of the MF (Rueckert et al. 1999):

$$\min_{MF}\left(S\left(I_i \circ MF_i, I_{ref}\right) + \sigma BE(MF_i) + \gamma JAC(MF_i)\right)$$

where I_i describe the MR image at the respiratory phase i and I_{ref} is the MR image at the reference motion state. The weighting for the additional penalty terms was selected as $\sigma = 0.4$ and $\gamma = 0.1$. The spline grid spacing was twice as large as the spatial image resolution and image registration was carried out with a pyramidal approach with four levels to ensure large and small deformation can be accurately determined.

End-expiration was selected as the reference motion state and MF described the transformation of voxels in each respiratory phase to this reference state. In contrast to affine motion models for the heart, the proposed non-rigid approach ensures accurate motion estimation in the entire FOV, i.e. not only of the heart. Figure 3b gives an overview of the MR motion estimation.

MR motion correction and image reconstruction

For the final MR image reconstruction, the motion information was included in a motion-corrected image reconstruction (MCIR) which provided a high-quality MR image using all the acquired k-space data (Batchelor et al. 2005). Spatial total variation regularization was added to suppress any residual undersampling artefacts (Cruz et al. 2016). MCIR provided 3D motion corrected images at three different echo times at end-expiration (Fig. 3b).

Calculation of respiratory-resolved dynamic AC maps

The MCIR images of the three echo times were separated into water and fat content using a quadratic pseudoboolean optimization (Berglund & Kullberg 2012). Based on fat, water, in-phase and out-of-phase information, the image content was classified into four different tissue types: soft tissue, fat tissue, lung and air. AC maps (AC_{MCIR}) were obtained by assigning literature based attenuation values to these tissue types (Martinez-Moller et al. 2009): soft tissue 0.1 cm^{-1}, fat tissue 0.09 cm^{-1}, lung tissue 0.02 cm^{-1} and air 0 cm^{-1}. In a final step, MF were used to transform the AC map to eight different respiratory motion states yielding AC_{Dyn}.

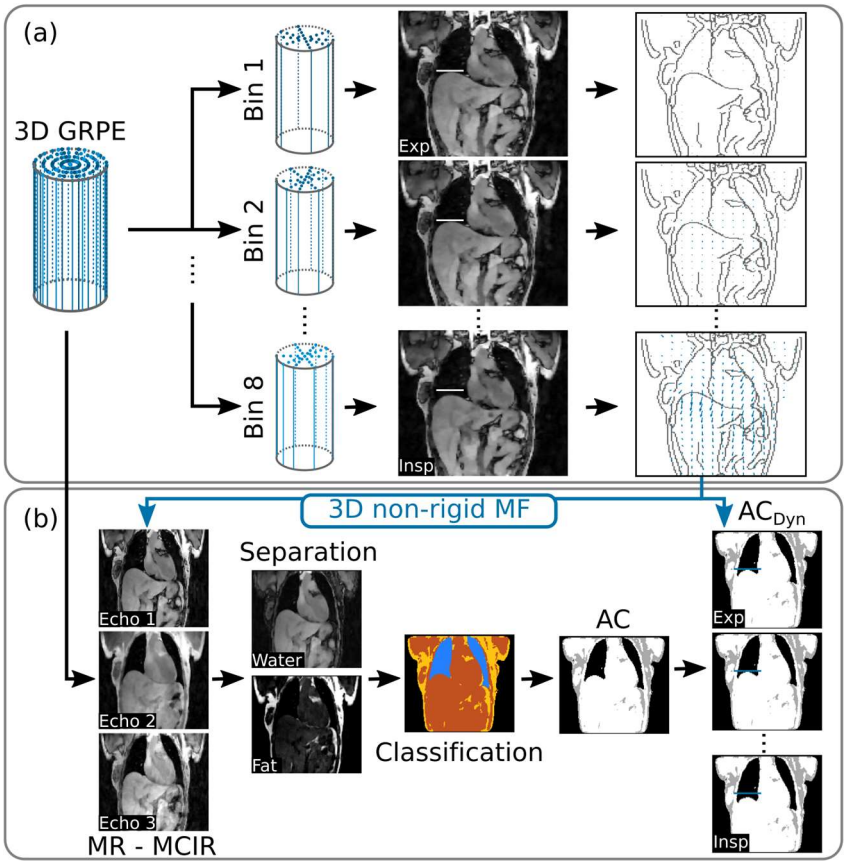

Figure 3: (a) MR motion estimation. The 3D GRPE data were split into eight respiratory bins using a self-navigator signal. 3D images at different respiratory phases were reconstructed and non-rigid motion fields (MF) were obtained by image-based registration. (b). Dynamic attenuation correction maps (AC_{Dyn}). MF were used in a motion-corrected MR image reconstruction (MR-MCIR) to obtain 3D images at three echo times. Based on these images, fat and water content was separated and tissue classification was carried out (yellow – fat, orange – soft tissue, blue – lungs, black – air). The classified tissue types were assigned literature-based AC values and MF were used to create dynamic AC maps. Exp expiration. Insp inspiration.

For comparison purposes, static AC maps were also obtained from GRPE-MR images without motion correction (AC_{Uncorr}).

PET motion correction and image reconstruction

MR-derived MF were also utilized in a motion-compensated PET image reconstruction to directly reconstruct respiratory motion corrected PET images in the reference motion state (i.e. end-expiration) (Qiao et al. 2006; Dey 2010). The MR-based 1D projections acquired every 750 ms were used as a respiratory motion surrogate to separate the PET list mode data into eight respiratory

motion states in the same way as the MR data. The MR-derived MF are then used during PET image reconstruction to transform all data to the same reference motion state. This yields a single motion corrected PET image reconstructed from all acquired PET data. Correction for scatter and random events was carried out for each respiratory motion state separately (Tsoumpas et al. 2004; Polycarpou et al. 2011).

PET images with a matrix size of 344 x 344 x 127 and a spatial resolution of 2.1 x 2.1 x 2.0 mm^3 were reconstructed using an iterative 3D ordered subsets expectation maximization algorithm (Thielemans et al. 2012). The reconstruction was carried out for three full iterations each with 23 subsets. Post-filtering with a 4 mm^3 isotropic 3D Gaussian kernel was applied.

The beating motion of the heart can also lead to strong blurring of cardiac ^{18}F-FDG PET images. Therefore, the PET list-mode data was cardiac gated to a 600 ms mid-diastolic window prior to image reconstruction, i.e. the list-mode data at systole was excluded. The cardiac gating was carried out based on an electrocardiogram signal recorded with an external MR-compatible electrocardiogram device. The beginning of each cardiac cycle defined by the R-peak was detected and PET data was only used for image reconstruction within a 600 ms window calculated with a fixed delay from the R-peak. For evaluation purposes PET images without motion correction (noMC) using the standard breathhold AC_{Stat} were reconstructed also with cardiac gating.

Respiratory motion can lead to blurring of uptake structures (blurring error) and misalignment between AC and PET emission data (AC error). In order to study these two effects separately, PET images without attenuation correction (noAC) were also reconstructed, leading to the following images for each patient:

- noAC-noMC: no attenuation correction and no respiratory motion compensation
- noAC-MCIR: no attenuation correction and respiratory MCIR
- AC_{Stat}-noMC: attenuation correction using AC_{Stat} and no respiratory motion compensation
- AC_{Dyn}-MCIR: attenuation correction using AC_{Dyn} and respiratory MCIR

AC information was not used for noAC images and therefore any difference between noAC-noMC and noAC-MCIR PET images was only due to the blurring error but not the AC error. Comparing the AC_{Stat}-noMC and AC_{Dyn}-MCIR images showed the combined effect of blurring and AC errors.

Quantitative evaluation

The respiratory motion amplitude was calculated as the length of the motion vectors between end-expiration and end-inspiration for all patients and evaluated in the standard 17 myocardial segments defined by the American Heart Association (Cerqueira et al. 2002).

In order to assess the effect of motion blurring on image resolution, the full-width-at-half-maximum (FWHM) and the maximum value of the uptake in the myocardium (UV_{max}) were compared between noAC-noMC and noAC-MCIR PET images for an inferior region in the heart. AC information was not used for noAC images and therefore any difference between noAC-noMC and noAC-MCIR PET images was only due to the blurring error but not the AC error. FWHM and UV_{max} were calculated by fitting a Gaussian curve to PET uptake profiles obtained from the inferior region of the heart in a long-axis view. The fitting procedure was used to make this evaluation more reproducible and less affected by noise. The average difference of FWHM and UV_{max} was determined over all profiles for each patient. In addition, the minimum and maximum difference was also calculated. This assessment was carried out in a few manually selected regions of the heart rather than for all 17 myocardial segments in order to ensure FWHM and UV_{max} only described the blurring of the myocardial PET signal and were not impaired by uptake from the papillary muscles.

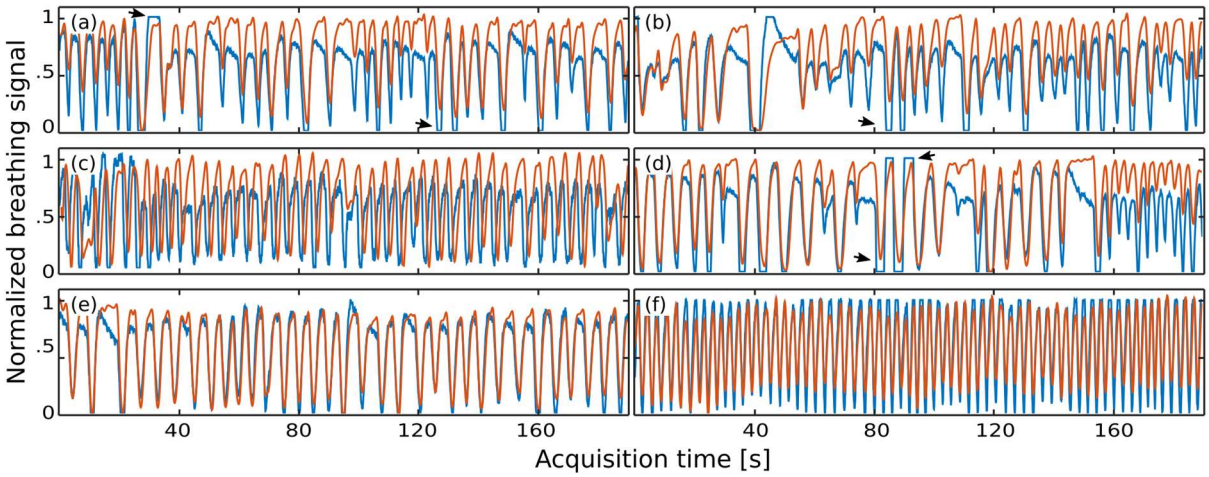

Figure 4: Comparison of MR-based self-navigator (red) and respiratory belt signal (blue) for all six patients (a-f). Strong in- and exhalation can lead to saturation of belt signal (arrows). In one patient (c) the foot-head motion of the heart obtained from the MR-based self-navigator is phase-shifted compared to the anterior-posterior motion of the chest wall and abdomen measured with the respiratory belt.

The combined effect of blurring and AC error was assessed by comparing the average uptake values (UV_{mean}) between AC_{Stat}-noMC and AC_{Dyn}-MCIR images. This quantitative evaluation was carried out again for the standard 17 myocardial segments.

An Anderson-Darling test was used to verify that all measured values follow a normal distribution and a two-tailed paired student's t-test was used to determine statistical significance for p-values smaller than 0.05.

RESULTS

A comparison between the obtained MR-based respiratory surrogate signals and the simultaneously recorded respiratory belt signals is shown in Figure 4. The breathing pattern varied strongly between patients and also within patients during the PET-MR scan. The respiratory belt was in good agreement with the obtained MR-based respiratory signal but suffered from signal saturation during deep inhalation and exhalation. In addition, one patient showed a phase shift between the MR-based surrogate and the respiratory belt signal. Figure 5 shows the results of the free-breathing triple-echo GRPE acquisition and the corresponding AC_{Dyn} maps. Respiratory motion caused blurring and ghosting

artefacts in the multi-echo MR images. The proposed MR-MCIR reconstruction compensated for those artefacts and led to a clear depiction of the cardiac anatomy and of the surrounding organs such as the liver. The respiratory resolved AC_{Dyn} shows the heart in different respiratory phases ensuring accurate alignment between AC information and free-breathing PET data. Figure 6 compares the AC maps obtained from the MR-MCIR images and the uncorrected MR images. Due to motion induced blurring and ghosting artefacts, the AC map obtained from the uncorrected MR images underestimates the extent of the heart compared to AC_{MCIR} corrected to end-expiration. For patient 1 motion artefacts in the lungs also leads to wrong classification of lung tissue as soft tissue. All of these artefacts would lead to signal errors in the final PET image.

An example of the combined effect of blurring and AC error is shown in Fig. 7. Misalignment between PET emission data and standard static AC maps (probably caused by a breathhold in inspiration rather than expiration) caused severe artefacts in the reconstructed PET images, because the anterior-lateral region of the myocardium was attenuation-corrected with the values of lung tissue rather than soft tissue (white arrows in Fig. 7). Due to the large differences between lung and soft-tissue AC values, the AC error dominated in that region. Acquiring the AC information during free-breathing ensured good alignment between PET and AC_{Dyn} and resulted in an increase in UV_{mean} by up to 168% in the anterior segments. In the inferior-septal region of the heart, the AC map was also misaligned with respect to the PET data, but due to the similar AC values of the heart and the surrounding tissue in that region, the AC error was small and the blurring error dominated (black arrows in Fig. 7). AC_{Dyn}-MCIR minimized the blurring error and led to an increase in UV_{mean} of more than 30% in this patient.

Short-axis and long-axis images as well as line plots of myocardial uptake comparing the standard approach to the proposed AC_{Dyn}-MCIR technique are shown in Fig. 8. AC_{Dyn}-MCIR increased the measured uptake and reduced motion blurring leading to a narrower profile of the myocardium. Small features such as the papillary muscles were more clearly depicted.

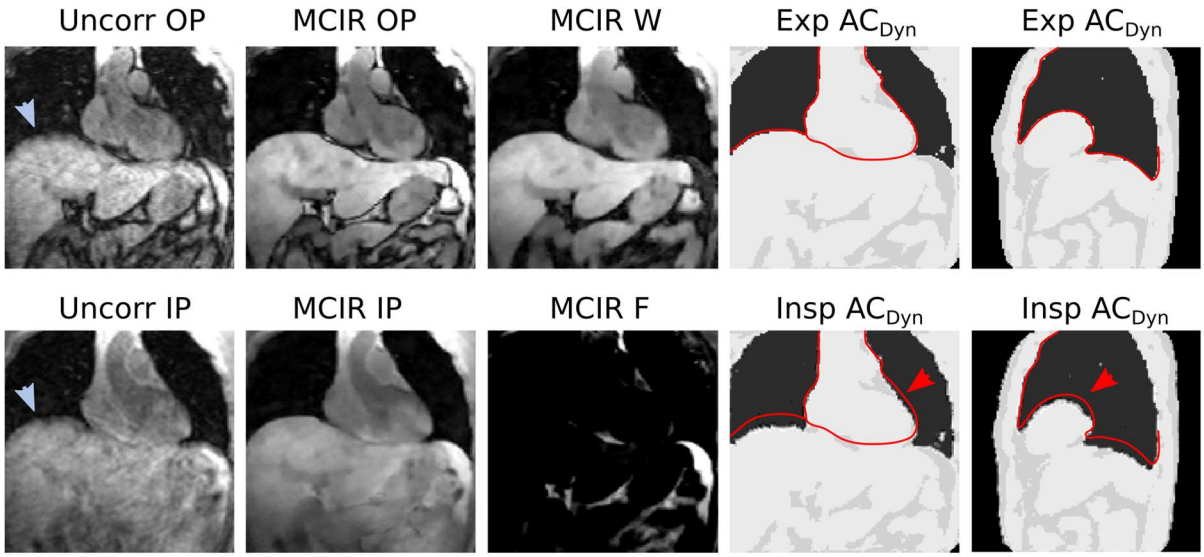

Figure 5: Respiratory-resolved AC_{Dyn}. Out-of-phase (OP) and in-phase (IP) GRPE images used for the separation of water (W) and fat (F) content. Based on these images, a tissue classification is carried out and dynamic attenuation correction (AC_{Dyn}) maps are calculated. Motion-corrected image reconstruction (MCIR) reduces motion artefacts such as blurring of the diaphragm (light blue arrow) compared to the uncorrected (Uncorr) images. AC maps are obtained for eight different respiratory phases. Differences of the cardiac anatomy between end-expiration (Exp) and end-inspiration (Insp) can be seen.

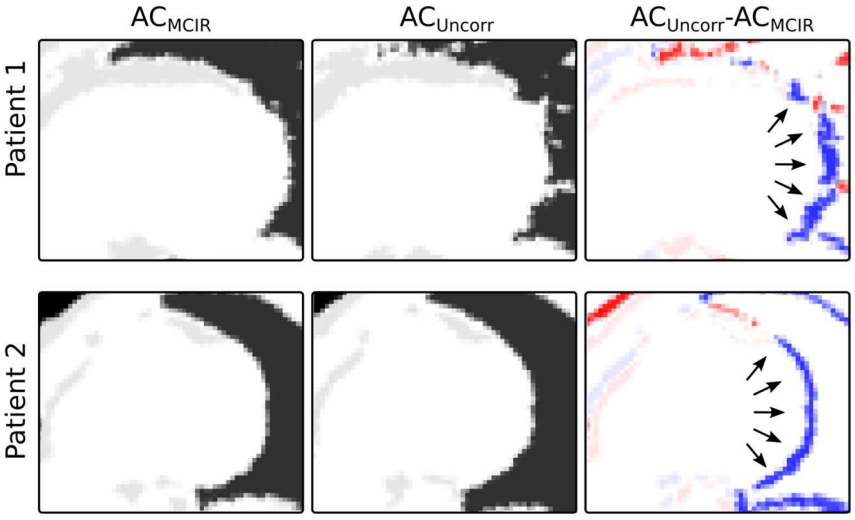

Figure 6: Comparison of AC map calculated from uncorrected MR images (AC_{Uncorr}) and MR images obtained with MCIR (AC_{MCIR}) for two patients. The difference images show that AC_{Uncorr} underestimates the outline of the heart due to respiratory motion blurring in the MR images. This is especially a problem where the heart borders to the lungs (black arrows).

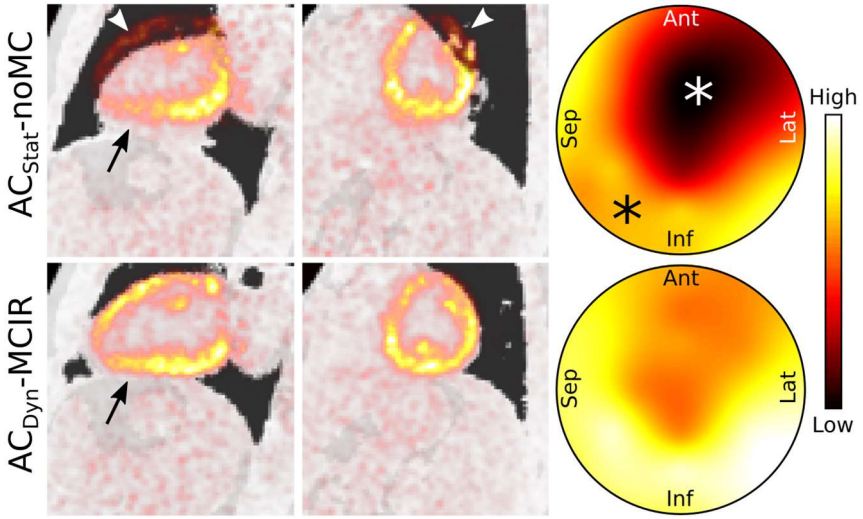

Figure 7: The standard approach (AC_{Stat}-noMC) led to quantification errors in the anterior-lateral area of the heart due to misalignment between PET emission data and AC_{Stat} maps (white arrows and white asterix). In the inferior region of the heart, blurring due to respiratory motion decreased measured uptake values (black arrows and black asterix). The proposed AC_{Dyn}-MCIR approach ensured accurate alignment between PET and AC data and reduced any motion induced blurring which significantly improved PET quantification.

Figure 9a,b show orientation and amplitude of the respiratory motion vectors between end-expiration and end-inspiration determined from the motion-resolved 3D MR data for a patient. The main motion direction in the heart was along the foot-head direction. That corresponded to a main motion direction from the anterior-anterolateral to the inferior-inferoseptal segments in the short-axis orientation. The amplitude of the motion was similar for the different heart regions with higher values in the inferior part of the mid-cavity slice (Fig. 9c) with an average of 8.2 ± 2.9 mm.

The reduced blurring of PET uptake in the myocardium was quantified by ΔFWHM shown in Table 1. PET-MCIR reduced motion-induced blurring of the myocardium by 20 ± 12% ($p<0.05$) with improvements of more than 40% in some patients. The peak uptake value UV_{max} was increased by 24 ± 5% ($p<0.05$) with maximum values between 40% and 50%.

The average increase in UV_{mean} for all patients is shown in Fig. 10. The comparison of the noAC PET images shows the improvement in UV_{mean} using MCIR due to a reduction of motion-induced blurring which is highest in the anterior-inferior and anterolateral-inferoseptal segments (Fig. 10a). Comparing UV_{mean} from AC_{Stat}-noMC to AC_{Dyn}-MCIR shows the combined effect of improved alignment

between PET emission data and AC maps and reduced motion artefacts (Fig. 10b). The highest improvements (between 30% and 40%) were in the anterior-lateral region.

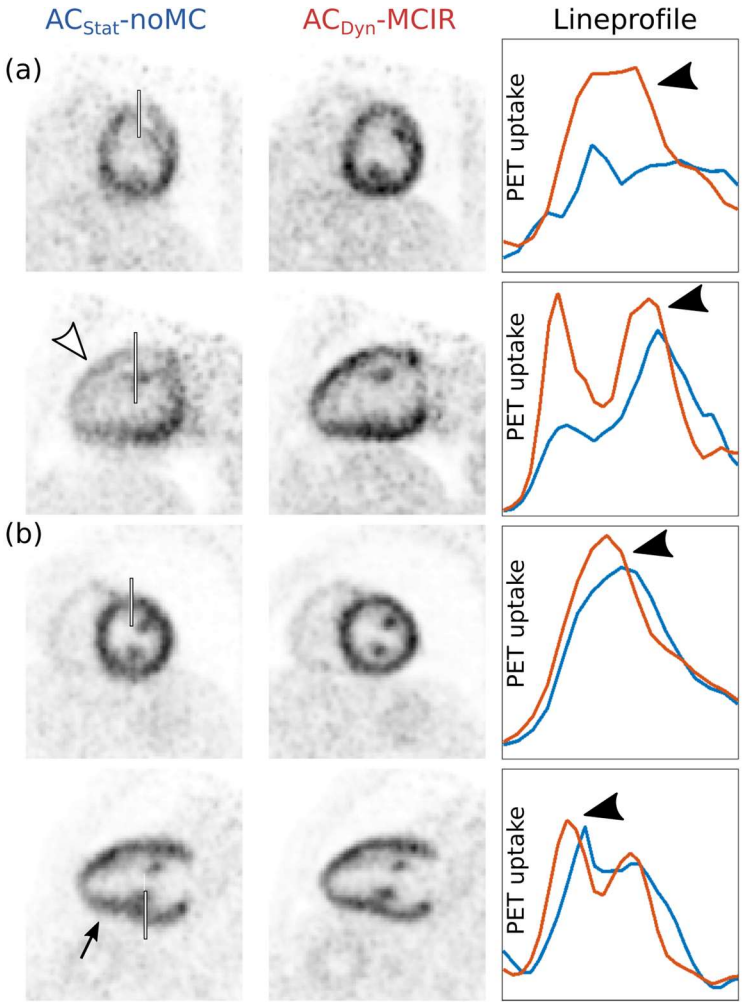

Figure 8 Improvement in image quality using the proposed technique (AC$_{Dyn}$-MCIR) compared to the standard approach (AC$_{Stat}$-noMC) for two patients (a,b). AC$_{Dyn}$-MCIR minimized motion induced blurring and improved uptake quantification (black arrows). Line profiles were drawn at positions marked with a rectangle in the PET images.

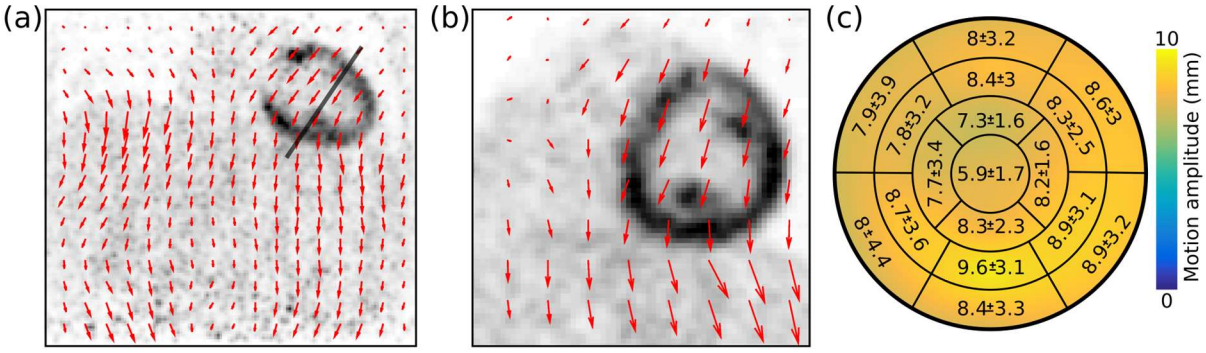

Figure 9. Respiratory motion orientation and amplitude. (a-b) Motion vectors between end-expiration and end-inspiration for a coronal (a) and short-axis (b) slice. The orientation of (a) is marked with a black line in (b). (c) Average motion amplitude and standard deviation.

Table 1: Respiratory motion amplitude and improvement in PET quantification.

Difference in peak uptake values (ΔUV_{max}) and full-width-at-half-maximum (ΔFWHM) of myocardial uptake measured between noAC-noMC and noAC-MCIR for all six patients. ΔUV_{max} and ΔFWHM are given as an average and min/max over several segments in the inferior part of the heart relative to noAC-noMC.

Patient	Motion amplitude [mm]	ΔUV_{max} [%]	ΔFWHM [%]
	Mean ± Std	Mean [Min Max]	Mean [Min Max]
1	10.2 ± 1.4	19 [3 42]	-23 [-55 4]
2	11.8 ± 2.0	29 [10 44]	-17 [-29 -5]
3	5.8 ± 0.9	27 [17 36]	-18 [-22 -3]
4	8.8 ± 2.0	22 [10 32]	-12 [-20 -4]
5	8.3 ± 1.4	27 [8 51]	-41 [-58 -29]
6	4.7 ± 0.8	17 [8 51]	-7 [-31 -8]

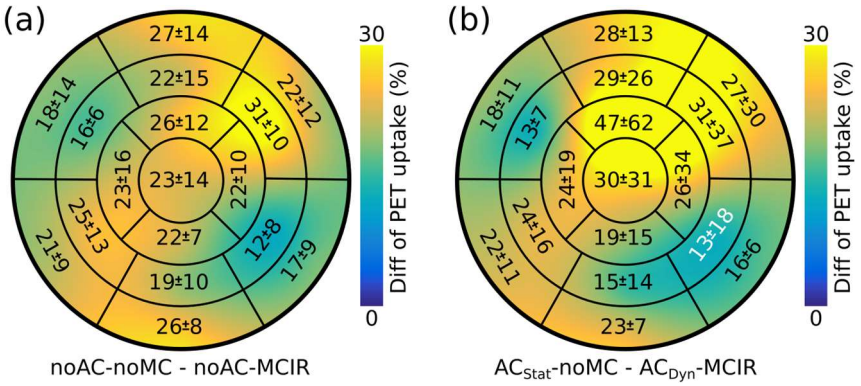

Figure 10 Relative difference of PET tracer uptake. (a) The increase of uptake using nonAC-MCIR compared to noAC-noMC is due to a reduced blurring error. (b) The increase of uptake using AC_{Dyn}-MCIR compared to AC_{Stat}-noMC is due to a reduced blurring error and reduced AC error. The increase of measured uptake was statistically significant ($p<0.05$) in all segments except for the mid inferolateral segment in (b).

DISCUSSION

The proposed AC_{Dyn}-MCIR approach provided respiratory resolved attenuation correction information which minimized quantification errors for free-breathing PET acquisitions. No breathhold acquisitions were required.

Respiratory motion amplitudes in the left ventricle were 8.2 ± 2.9mm which is in good agreement with previous studies on respiratory heart motion (Boucher et al. 2004; Scott et al. 2009; Schwaiger et al. 2005). The blurring error depends on the motion amplitude and also on the direction of motion relative to the heart. If the breathing motion is parallel to the myocardium and if the myocardium has a continuous uptake without any visible pathology, the blurring effect is small but if the breathing motion is perpendicular to the myocardium, the blurring effect is large. The orientation of the motion shown in Fig. 8a,b was similar for all patients, leading to larger motion effects on UV_{mean} in the anterior-anterolateral and inferior-inferoseptal segments of the heart (Fig. 9a) which has also been reported by Yu et al. (Yu et al. 2016; Boucher et al. 2004). The blurring effect of motion varies for different areas of the myocardium and also depends on the breathing pattern of the patient during the examination. Without motion correction the measured PET uptake signal can strongly differ and hence make it more challenging to detect areas with pathological uptake. Furthermore, follow up

examination can also be impaired, because changes in PET uptake can not only occur because of treatment but also because of a change in breathing.

In addition, the effect of respiratory motion on the measured PET uptake depends not just on the amplitude and orientation of the motion, but also on the breathing pattern (e.g. how much time is spent in end-expiration and end-inspiration) of the patient during data acquisition. This probably explains why there does not seem to be a clear correlation between motion amplitude and ΔFWHM and ΔUV_{max} in Tab. 1.

For the attenuation corrected PET images UV_{mean} was further increased using AC_{Dyn}-MCIR, especially in the anterior and anterolateral region of the heart (Fig. 9b). For these segments, the heart borders to the lungs. Therefore, any misalignment of AC and PET emission data caused severe quantification errors which were corrected for with AC_{Dyn}-MCIR. The strength of this effect depends on the misalignment between AC_{Stat} and PET emission data and therefore varies strongly between patients leading to high standard deviation. Previous studies on MR-based motion correction for PET have manually or automatically modified AC maps acquired during a breathhold to improve the alignment between AC and PET emission data, but did not assess the effect of the misalignment on the final PET image quantification (Furst et al. 2015; Dutta et al. 2015; Manber et al. 2016; Kolbitsch et al. 2017). Cardiac PET-CT studies, where the AC map is also acquired during a breathhold before or after the free-breathing PET emission scan (Schwaiger et al. 2005; Nye et al. 2007; Lautamäki et al. 2008). In those studies, misalignment problems between PET emission data and AC maps occurred in more than 60% of patients leading to quantification errors of more than 20% which is in agreement to our findings.

In this study MCIR was carried out by separating PET listmode data into eight respiratory motion states without taking inter- and intracycle variations of the breathing pattern into account. Nevertheless, using the MR-based self-navigator a continuous non-rigid motion model could also be created, which provides a specific motion transformation for each PET event (Chan et al. 2018).

The main limitation of this study is the small number of patients and further studies with a larger cohort of patients are required to obtain a better statistical description. The patients in this study were not cardiac PET patients, which ensured homogeneous uptake in the healthy myocardium and allowed a detailed assessment of the AC and blurring error in all segments. Nevertheless, further assessment on patients with pathological myocardial uptake is necessary.

In order to be able to bin the PET emission data in the same way as the MR raw data, a 1D MR respiratory surrogate signal was acquired every 750 ms. This short 6 ms acquisition could be easily integrated in a wide range of cardiac sequences. In contrast to a respiratory belt, which measures the movement of the abdominal or chest wall, that surrogate provided a direct displacement measure of respiratory heart motion and is not impaired by signal saturation or phase shifts between anterior-posterior motion of the thorax and the dominant foot-head motion of the heart. Nevertheless, a range of different techniques have been proposed, which obtain a respiratory surrogate signal directly from the PET data and would not require any additional MR data acquisition (Cal-González et al. 2017; Manber et al. 2015; Ren et al. 2017).

CONCLUSION

We have presented a novel approach which obtained dynamic AC and respiratory motion information during a short 75s free-breathing MR acquisition. The dynamic AC_{Dyn} data ensured accurate alignment between AC and PET data and respiratory motion information could be utilized in MCIR to reduce motion artefacts due to breathing for MR and PET images. Respiratory motion amplitudes of 8.2 ± 2.9 mm were measured in patients with a common motion orientation along the anterior-anterolateral and inferior-inferoseptal axis of the heart. MCIR AC_{Dyn} improved PET quantification significantly by 24 ± 5% and PET image resolution by 20 ± 12%. This will allow for more reproducible clinical assessment of the PET uptake in the myocardium and will also enable the visualization of small uptake features.

ACKNOWLEDGEMENT

Dr. Neji and Dr. Fenchel are employees of Siemens Healthineers. This work was part of the SUBLIMA project supported by the European Union under the seventh framework program (no: 241711). This research was supported by the National Institute for Health Research (NIHR) Biomedical Research Centre at Guy's and St Thomas' NHS Foundation Trust and King's College London. The views expressed are those of the authors and not necessarily those of the NHS, the NIHR or the Department of Health. The PET image reconstruction used for this project was in part developed during the Computational Collaborative Project in Synergistic PET-MR Reconstruction (https://www.ccppetmr.ac.uk/), UK EPSRC grant EP/M022587/1. The authors would also like to thank James Stirling and Sami Jeljeli for their help with the patient scanning.

REFERENCES

Aitken, A.P. et al., 2015. 100% Efficient three-dimensional coronary MR angiography with two-dimensional beat-to-beat translational and bin-to-bin affine motion correction. *Magnetic Resonance in Medicine*, 74(3), hal.756–764.

Batchelor, P.G. et al., 2005. Matrix description of general motion correction applied to multishot images. *Magnetic Resonance in Medicine*, 54(5), hal.1273–1280.

Bengel, F.M. et al., 2009. Cardiac Positron Emission Tomography. *Journal of the American College of Cardiology*, 54(1), hal.1–15.

Berglund, J. & Kullberg, J., 2012. Three-dimensional water/fat separation and T 2 * estimation based on whole-image optimization-Application in breathhold liver imaging at 1.5 T. *Magnetic Resonance in Medicine*, 67, hal.1684–1693.

Boucher, L. et al., 2004. Respiratory gating for 3-dimensional PET of the thorax: feasibility and initial results. *Journal of nuclear medicine : official publication, Society of Nuclear Medicine*, 45(2), hal.214–9.

Buerger, C., Prieto, C. & Schaeffter, T., 2013. Highly efficient 3D motion-compensated abdomen MRI from undersampled golden-RPE acquisitions. *Magma: Magnetic Resonance Materials in Physics, Biology, and Medicine*, 26(5), hal.419–429.

Cal-González, J. et al., 2017. Impact of motion compensation and partial volume correction for 18 F-NaF PET/CT imaging of coronary plaque. *Physics in Medicine & Biology*, 63(1), hal.15005.

Cerqueira, M.D. et al., 2002. Standardized Myocardial Segmentation and Nomenclature for Tomographic Imaging of the Heart. *Circulation*, hal.539–542.

Chan, C. et al., 2018. Non-Rigid Event-by-Event Continuous Respiratory Motion Compensated List-Mode Reconstruction for PET. *IEEE Transactions on Medical Imaging*, 37(2), hal.504–515.

Cruz, G. et al., 2016. Accelerated motion corrected three-dimensional abdominal MRI using total variation regularized SENSE reconstruction. *Magnetic Resonance in Medicine*, 75(4), hal.1484–

1498.

Dey, J., 2010. Reconstruction Algorithms for Motion Correction in Emission. *IEEE Trans Nucl Sci.*, 56(5), hal.2739–2749.

Dutta, J. et al., 2015. Pulmonary imaging using respiratory motion compensated simultaneous PET/MR. *Medical Physics*, 42(7), hal.4227–4240.

Furst, S. et al., 2015. Motion Correction Strategies for Integrated PET/MR. *Journal of Nuclear Medicine*, 56(2), hal.261–269.

Grimm, R. et al., 2015. Self-gated MRI motion modeling for respiratory motion compensation in integrated PET/MRI. *Medical Image Analysis*, 19(1), hal.110–120.

Kolbitsch, C. et al., 2017. Cardiac and Respiratory Motion Correction for Simultaneous Cardiac PET/MR. *Journal of Nuclear Medicine*, 58(5), hal.846–852.

Kolbitsch, C. et al., 2018. Fully integrated 3D high-resolution multicontrast abdominal PET-MR with high scan efficiency. *Magnetic Resonance in Medicine*, 79(2), hal.900–911.

Lautamäki, R. et al., 2008. CT-based attenuation correction in 82Rb-myocardial perfusion PET-CT: Incidence of misalignment and effect on regional tracer distribution. *European Journal of Nuclear Medicine and Molecular Imaging*, 35(2), hal.305–310.

Loghin, C., Sdringola, S. & Gould, K.L., 2004. Common Artifacts in PET Myocardial Perfusion Images Due to Attenuation–Emission Misregistration: Clinical Significance, Causes, and Solutions. *Journal of Nuclear Medicine*, 45(6), hal.1029–1039.

Manber, R. et al., 2016. Joint PET-MR respiratory motion models for clinical PET motion correction. *Physics in Medicine and Biology*, 61(17), hal.6515–6530.

Manber, R. et al., 2015. Practical PET Respiratory Motion Correction in Clinical PET/MR. *Journal of Nuclear Medicine*, 56(6), hal.890–896.

Martinez-Moller, A. et al., 2009. Tissue Classification as a Potential Approach for Attenuation Correction in Whole-Body PET/MRI: Evaluation with PET/CT Data. *Journal of Nuclear Medicine*,

50(4), hal.520–526.

Martinez-Moller, A. et al., 2012. Workflow and Scan Protocol Considerations for Integrated Whole-Body PET/MRI in Oncology. *Journal of Nuclear Medicine*, 53(9), hal.1415–1426.

Munoz, C. et al., 2018. Motion-corrected simultaneous cardiac positron emission tomography and coronary MR angiography with high acquisition efficiency. *Magnetic Resonance in Medicine*, 79(1), hal.339–350.

Nye, J.A., Esteves, F. & Votaw, J.R., 2007. Minimizing artifacts resulting from respiratory and cardiac motion by optimization of the transmission scan in cardiac PET/CT. *Medical Physics*, 34(6), hal.1901–1906.

Pang, J. et al., 2014. ECG and navigator-free four-dimensional whole-heart coronary MRA for simultaneous visualization of cardiac anatomy and function. *Magnetic Resonance in Medicine*, 72(5), hal.1208–1217.

Polycarpou, I. et al., 2011. Comparative evaluation of scatter correction in {3D PET} using different scatter-level approximations. *Ann Nucl Med*, 25(9), hal.643–649.

Prieto, C. et al., 2010. 3D Undersampled Golden-Radial Phase Encoding for DCE-MRA Using Inherently Regularized Iterative SENSE. *Magnetic Resonance Imaging*, 64, hal.514–526.

Pruessmann, K.P. et al., 2001. Advances in sensitivity encoding with arbitrary k-space trajectories. *Magnetic Resonance Imaging*, 46(4), hal.638–651.

Qiao, F. et al., 2006. A motion-incorporated reconstruction method for gated PET studies. *Phys Med Biol*, 51(15), hal.3769–3783.

Ren, S. et al., 2017. Data-driven event-by-event respiratory motion correction using TOF PET list-mode centroid of distribution. *Physics in Medicine and Biology*, 62(12), hal.4741–4755.

Rueckert, D. et al., 1999. Nonrigid registration using free-form deformations: application to breast MR images. *IEEE Transactions on Medical Imaging*, 18(8), hal.712–721.

Schwaiger, M., Ziegler, S. & Nekolla, S.G., 2005. PET/CT: challenge for nuclear cardiology. *Journal of*

nuclear medicine : official publication, Society of Nuclear Medicine, 46(10), hal.1664–78.

Scott, A.D., Keegan, J. & Firmin, D.N., 2009. Motion in cardiovascular MR imaging. *Radiology*, 250(2), hal.331–351.

Thielemans, K. et al., 2012. STIR: software for tomographic image reconstruction release 2. *Phys Med Biol*, 57(4), hal.867–883.

Tsoumpas, C. et al., 2004. Evaluation of the Single Scatter Simulation Algorithm Implemented in the STIR Library. In *IEEE Symposium Conference Record Nuclear Science 2004.* IEEE, hal. 3361–3365.

Yu, Y. et al., 2016. Event-by-Event Continuous Respiratory Motion Correction for Dynamic PET Imaging. *Journal of Nuclear Medicine*, 57(7), hal.1084–1090.